Check for updates

Advanced Functional Materials

ADVANCED FUNCTIONAL MATERIALS
www.afm-journal.de

RESEARCH ARTICLE OPEN ACCESS

Direct Integration of Conductive, Emissive Perovskite Nanocrystals Into Efficient Light-Emitting Diodes Without Post-Synthetic Ligand Exchange

Jigeon Kim[1] | Yubin Lee[1] | Gyeong Eun Seok[2] | Dong Gyu Lee[3,4] | Seongwon Lee[3] | Huieun Kim[1] | Sung Woo Jang[5] | Wooyeon Kim[6] | Wondo Choi[7] | Woo Hyeon Jeong[2] | Donghun Lee[1] | Min Jae Ko[6] | Won Bin Im[5] | Jinhan Cho[7] | Tae Kyung Lee[3,4] | Bo Ram Lee[2] | Younghoon Kim[1]

[1]Department of Chemistry, Kookmin University, Seoul, Republic of Korea | [2]School of Advanced Materials Science and Engineering, Sungkyunkwan University, Suwon, Republic of Korea | [3]Department of Organic and Nano Engineering, Hanyang University, Seoul, Republic of Korea | [4]Human-Tech Convergence Program, Hanyang University, Seoul, Republic of Korea | [5]Division of Materials Science and Engineering, Hanyang University, Seoul, Republic of Korea | [6]Department of Chemical Engineering, Hanyang University, Seoul, Republic of Korea | [7]Department of Chemical and Biological Engineering, Korea University, Seoul, Republic of Korea

Correspondence: Tae Kyung Lee (tklee@hanyang.ac.kr) | Bo Ram Lee (brlee@skku.edu) | Younghoon Kim (younghoon.kim@kookmin.ac.kr)

Received: 4 February 2026 | **Revised:** 28 June 2026 | **Accepted:** 4 August 2026

Keywords: charge carrier | colloid | diode | electron mobility | materials science | nanocrystal | optoelectronics | perovskite | quantum efficiency | thin film

ABSTRACT

Colloidal perovskite nanocrystals (PNCs) have emerged as promising candidates for optoelectronic applications, leveraging their excellent optical, photophysical, and electrical properties combined with solution processability. However, the electrically insulating nature of conventional long-chain ligands necessitates post-synthetic ligand exchange for practical device integration. Here, we demonstrate that a synthetically engineered surface chemistry, featuring a low ligand density and robust halide passivation, enables the direct integration of colloidal PNCs into optoelectronic devices without a ligand exchange process. This is achieved by synthesizing $CsPbBr_3$ PNCs stabilized with Br^- instead of anionic oleate ligands. Due to the stronger binding of the OAM/Br^- ligand system to the $CsPbBr_3$ surface, compared to the OAM/oleate system, the resultant PNCs show suppressed surface defect formation and improved optical properties. The reduced surface ligand density allows for higher charge carrier mobility in the PNC thin films relative to their oleate-capped counterparts. Without post-synthetic ligand exchange, the colloidal PNCs are directly integrated into light-emitting diodes, achieving enhanced charge carrier injection and a higher maximum external quantum efficiency of 11.4%, compared to 2.7% for conventional PNC-based devices.

1 | Introduction

Inorganic semiconductor nanocrystals (NCs), including quantum dots (QDs), are of great interest in optoelectronic applications owing to their size- and dimension-tunable optical bandgap energy (E_g), which arises from the quantum confinement effect, and high photoluminescence quantum yield (PLQY) [1]. In addition, their optical and electrical properties can be enhanced through precise control of surface chemistry and engineering across the diverse exposed facets on the surface [2]. Colloidal NCs, synthesized via wet-chemical synthetic routes, enable further advanced solution processability for room-temperature,

Jigeon Kim, Yubin Lee, and Gyeong Eun Seok contributed equally to this work.

This is an open access article under the terms of the Creative Commons Attribution-NonCommercial-NoDerivs License, which permits use and distribution in any medium, provided the original work is properly cited, the use is non-commercial and no modifications or adaptations are made.
© 2026 The Author(s). *Advanced Functional Materials* published by Wiley-VCH GmbH

large-area device fabrication [3]. Among these materials, lead-halide perovskite colloidal NCs (PNCs) have recently emerged as exceptional candidates. They exhibit outstanding PLQY and color purity without complex core–shell nanostructures due to their unique defect tolerance, and efficient ambipolar charge transport [4, 5]. They also satisfy the RGB color gamut proposed by Rec. 2020 by tuning their crystal size, dimension, and halide compositions [6]. These advantageous properties position PNCs as leading candidates for the emissive layers in high-performance light-emitting diodes (LEDs), comparable to conventional organic and QD-based LEDs [7].

Conventional colloidal syntheses, such as the hot-injection (HI) method, rely on long-chain hydrocarbon ligands (e.g., oleic acid (OA), oleylamine (OLA), etc.) to produce high quality and monodisperse PNCs [8]. These long-chain organic ligands are essential, stabilizing the PNC surface to reduce surface defects and controlling crystal growth to ensure high monodispersity [2]. These two factors directly influence their optical and photophysical properties, which are involved in the performance and stability of PNC-based devices [9, 10]. Furthermore, these long-chain ligands provide colloidal dispersibility in nonpolar organic solvents, allowing PNCs to be utilized as a colloidal ink. The surfaces of PNCs are typically stabilized using a combination of anionic oleate originating from deprotonated OA and cationic oleylammonium (OAM) derived from protonated OLA [8]. It is understood that OAM ligands participate as A-site cations on the (100) facets of the perovskite lattice [11]. By contrast, although oleate ligands are known to bind to surface metal cations, the extent to which they contribute to surface passivation and their exact binding behavior are still subjects of ongoing discussion [12]. However, the electrically insulating nature of the long-chain ligands creates a bottleneck to the integration of the as-synthesized PNCs in high-performance devices by impeding charge transport within the as-cast solids, thus necessitating their removal [9].

To address this challenge, post-treatment ligand exchange processes have widely been adopted as an indispensable solution [9]. This ligand exchange step, performed either in the solid-state or solution-phase, replaces the long-chain, insulating ligands with shorter, more conductive species (e.g., atoms, molecules). Therefore, these ligand exchange processes, an additional step performed either before or after PNC coating, have enhanced charge transport within PNC-based thin films, thereby enabling the development of high-performance optoelectronic devices [13]. The rapid development of PNC-based optoelectronic devices has been driven by advances in post-synthetic ligand exchange strategies [12, 13]. The necessity for the ligand exchange inherently stems from the synthesis process itself, which yields PNCs capped with long-chain surface ligands. Various colloidal synthetic routes have been developed to reinforce organic ligand passivation, aiming to improve the optical properties and the colloidal stability of PNCs [14]. However, once sufficient colloidal dispersibility is achieved, an excessively high density of long-chain ligands is no longer necessary. Therefore, it is desirable to synthetically engineer the surface chemistry to suppress surface defects through precise, robust atomic passivation, rather than relying on a larger amount of insulating species.

Herein, we demonstrate that an atomic-level surface chemistry, featuring a low ligand density and robust halide passivation, enables colloidal PNCs to yield highly conductive and emissive thin films, allowing for direct integration into LEDs without requiring any post-synthetic ligand exchange. We synthesize $CsPbBr_3$ PNCs with a low ligand density via a bimolecular nucleophilic substitution (S_N2)-based heat-up method (denoted as HU-PNCs). In contrast to PNCs synthesized via the conventional HI method (denoted as HI-PNCs), the HU-PNCs exhibit an absence of oleate ligands, a finding confirmed by chemical and thermal analysis. Nevertheless, HU-PNCs exhibit colloidal dispersibility in non-polar organic solvents. The surface stabilization of the HU-PNCs by the OAM/Br^- ligand system, which exhibits a higher binding energy (E_b) than the OAM/oleate system, results in suppressed surface defect formation and increased PLQY. Furthermore, the HU-PNCs exhibit improved crystal size uniformity compared to HI-PNCs, which leads to suppressed energetic disorder, enhanced orientational ordering, and a narrower emission bandwidth in solid-state thin films. Enabled by their inherently low-ligand-density surface chemistry, the HU-PNC thin films show higher charge carrier mobility compared to HI-PNC thin films, without requiring any post-synthetic ligand exchange. Consequently, the HU-PNC-based emissive layers were directly applied to LEDs, exhibiting improved charge injection and a maximum external quantum efficiency (EQE_{max}) of 11.4% compared to 2.7% for the HI-PNC-based devices.

2 | Results and Discussion

The conventional HI synthesis involves the injection of chemically distinct precursor solutions at high temperatures, which can complicate the precise temporal separation of nucleation and crystal growth stages (Figure 1a). Furthermore, the surface chemistry of as-synthesized HI-PNCs is widely reported, in which they are passivated by anionic oleate and cationic OAM ligands, typically requiring purification with polar anti-solvents and subsequent ligand exchange processes to facilitate their integration into optoelectronic devices [15]. In contrast, the S_N2-based HU synthesis utilizes the S_N2 reaction of alkyl halides to decouple the supply of halide sources from metal precursors (Figure 1a). This approach modulates precursor reactivity, thereby regulating the nucleation and crystal growth in the colloidal synthetic system, enabling HU-PNCs to achieve superior size uniformity compared to HI-PNCs [6]. Therefore, HU-PNCs exhibit suppressed energy disorder, suggesting higher potential in device applications. To exploit this potential for direct integration into optoelectronic devices, it is essential to first elucidate their surface chemistry in comparison to that of conventional HI-PNCs. To systematically compare these two approaches, we synthesized both HI- and HU-$CsPbBr_3$ PNCs and subjected them to a conventional purification protocol using methyl acetate (MeOAc) as a polar anti-solvent (see details in Methods) [16].

The as-synthesized HI- and HU-PNCs were isolated from the crude solutions via high-speed centrifugation prior to the MeOAc-based purification process. High-resolution transmission electron microscopy (HR-TEM) images revealed that the as-isolated HU-PNCs showed a highly monodisperse morphology compared to

16163028, 2026, 75, Downloaded from https://advanced.onlinelibrary.wiley.com/doi/10.1002/adfm.77751 by Hanyang University Library, Wiley Online Library on [08/11/2026]. See the Terms and Conditions (https://onlinelibrary.wiley.com/terms-and-conditions) on Wiley Online Library for rules of use; OA articles are governed by the applicable Creative Commons License

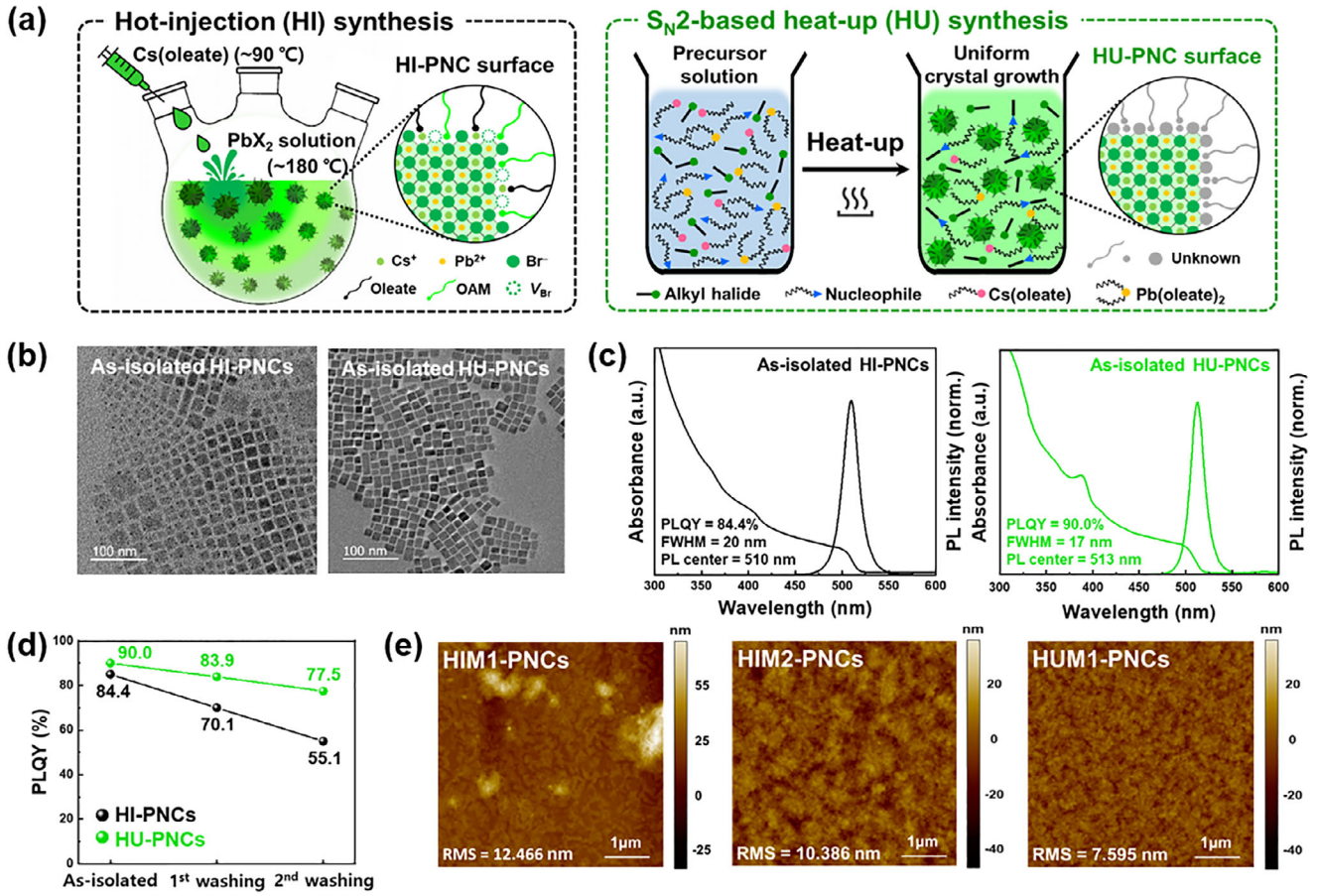

FIGURE 1 | (a) Schematic illustrations showing conventional HI and S_N2-based HU synthesis. The S_N2 reactions of alkyl bromide (R–Br), promoted by nucleophiles such as oleate and OLA, can be described by the following equations: [R–Br + 2OLA → secondary amine + OAM–Br] and [R–Br + oleate + OAM → ester + OAM–Br]. (b) HR-TEM images and (c) UV–Vis absorption and PL spectra of as-isolated HI- and HU-PNCs. (d) Solution-phase PLQY values of HU- and HI-PNCs isolated using high-speed centrifugation before purification, and after subsequent purifications with MeOAc once and twice (i.e., HIM1-, HIM2-, HUM1-, and HUM2-PNCs). (e) AFM images of spin-cast thin films composed of HIM1-, HIM2-, and HUM1-PNCs.

the as-isolated HI-PNCs (Figure 1b). The as-isolated HU-PNCs exhibited a higher solution-phase PLQY of 90.0% and a narrower full width at half maximum (FWHM) of 17 nm, compared to 84.4% and 20 nm observed for the as-isolated HI-PNCs, respectively (Figure 1c). This enhancement is attributed to the lower energy disorder and minimized energy loss inherent to the monodisperse HU-PNCs, compared to HI-PNCs [6]. The HU-PNCs, purified with MeOAc once and twice (denoted as HUM1- and HUM2-PNCs, respectively), also showed higher PLQYs and narrower FWHM values compared to those of the HI-PNCs purified under identical conditions (denoted as HIM1- and HIM2-PNCs, respectively) (Figure 1d and Figure S1). However, HIM2- and HUM2-PNCs exhibited lower PLQY values compared to HIM1- and HUM1-PNCs, respectively. This reduction is attributed to ligand loss and subsequent surface defect formation induced by the polar MeOAc anti-solvent [17].

We fabricated PNC-based thin films by spin-coating the purified HI- and HU-PNC solutions, and subsequently investigated their surface morphology through atomic force microscopy (AFM) measurements. The HIM1-PNC thin film exhibited a high root mean square (RMS) roughness of 12.466 nm characterized by an aggregated morphology, whereas the HIM2-PNC thin film showed a smoother surface with a lower RMS roughness of 10.386 nm (Figure 1e). Particularly, optical microscopy images revealed the formation of an oily residue on the HIM1-PNC thin film, which is attributed to residual long-chain hydrocarbon ligands and solvent (Figure S2). However, the HUM1-PNC thin film exhibited a uniform surface morphology and a low RMS roughness of 7.595 nm, even when prepared using the once-purified PNC solution (Figure 1e). These results indicate that obtaining high-quality, uniform HI-PNC thin films requires purification process at least twice, inevitably compromising their optical properties. In contrast, HU-PNCs yield high-quality thin films with only a single purification step.

We performed thermogravimetric analysis (TGA) and proton nuclear magnetic resonance (^{1}H-NMR) spectroscopy on the HI- and HU-PNCs to determine whether residual ligands and solvents contributed to the difference in thin film morphology observed at varying purification steps. The TGA plots revealed that HIM1-PNCs exhibited a weight loss of 32% at 430 °C, significantly higher than the 20% and 12% observed for HIM2- and HUM1-PNCs, respectively (Figure 2a) [18]. This indicates a substantially higher residual organic content in the HIM1-PNCs. The ^{1}H-NMR spectra of both the as-isolated HI-PNCs and HIM1-PNCs displayed C═C resonance peaks at 4.95 and 5.80 ppm corresponding to 1-octadecene (ODE), which is used as a solvent in HI synthesis

16163028, 2026, 75, Downloaded from https://advanced.onlinelibrary.wiley.com/doi/10.1002/adfm.77751 by Hanyang University Library, Wiley Online Library on [08/11/2026]. See the Terms and Conditions (https://onlinelibrary.wiley.com/terms-and-conditions) on Wiley Online Library for rules of use; OA articles are governed by the applicable Creative Commons License

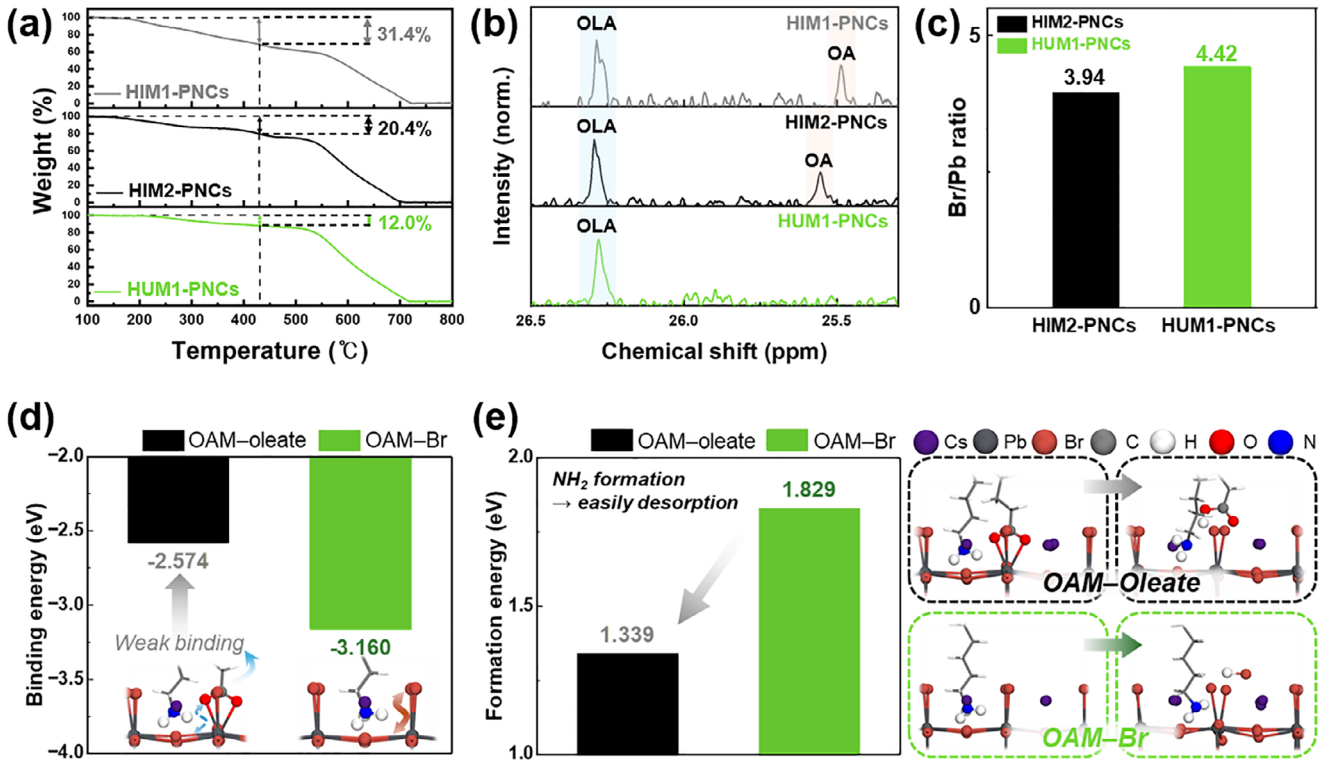

FIGURE 2 | (a) TGA plots and (b) ^{13}C-NMR spectra of HIM1-, HIM2 and HUM1-PNCs. (c) Surface Br/Pb elemental ratios of HIM2- and HUM1-PNCs obtained from XPS measurements. (d) E_b of the surface models containing OAM and oleate, and OAM and Br^-, on the (100) surface of $CsPbBr_3$ perovskite. (e) Formation energies of the deprotonation reaction of OAM in the presence of oleate or Br^- on the (100) surface of $CsPbBr_3$ perovskite.

(Figure S3). This suggests that the presence of residual ODE is responsible for the oily residue observed in the HIM1-PNC thin films, as it is the most abundant oily species in the HI synthesis and remains non-volatile at the reaction temperature. The ^{1}H-NMR spectrum of the HIM2-PNCs exhibited no C═C resonances at 4.95 and 5.80 ppm, suggesting that a uniform PNC thin film with low RMS roughness was formed. In contrast, the ^{1}H-NMR spectrum of the HUM1-PNCs showed no resonances associated with residual precursors (e.g., 1-octyl bromide) that were present in the as-isolated HU-PNCs (Figure S4) [6]. These results demonstrate that a single purification step is sufficient to fabricate high-quality and uniform PNC thin films using HU-PNC solution synthesized in the absence of non-volatile ODE.

These findings are also supported by Fourier-transform infrared (FT-IR) and carbon-13 NMR (^{13}C-NMR) spectroscopy. The FT-IR spectrum of HIM1-PNCs showed stronger and higher C–H stretching vibrations (2800–3030 cm^{-1}) arising from residual ODE, compared to that of HIM2-PNCs (Figure S5). However, the FT-IR spectrum of HUM1-PNCs exhibited weaker and lower C–H stretching vibrations and negligible carboxylate stretching signals (i.e., symmetric and asymmetric COO^-) originating from oleate, compared to that of the HI-PNCs. Particularly, while the ^{13}C-NMR spectra of both HIM1- and HIM2-PNCs exhibited distinct resonances at ~25.5 ppm characteristic of oleate ligands, these signals were absent in the ^{13}C-NMR spectrum of HUM1-PNCs (Figure 2b and Figure S6). This further suggests that, unlike HI-PNCs, the surfaces of HU-PNCs are stabilized predominantly by cationic OAM ligands, with minimal contribution from anionic oleate ligands. These results can be explained by the fact that oleate functions primarily as a nucleophile in the S_N2 reaction. Before the onset of nucleation and crystal growth, it contributes to the formation and accumulation of the halide precursor, OAM bromide (OAM–Br) (Figure S7) [6]. Consequently, OAM plays a dominant role in the final ligand environment of the HU-PNCs. Based on these differences in surface ligands, we calculated the ligand densities of the HIM2- and HUM1-PNCs (Note S1). The calculated ligand density of the HUM1-PNCs was approximately 34.6% lower than that of the HIM2-PNCs (Table S1).

As shown in Figure 1d, HUM1-PNCs exhibited higher PLQY values than HIM2-PNCs, even in the absence of anionic oleate ligands. To elucidate the origin of this enhanced optical property, we performed X-ray photoelectron spectroscopy (XPS) measurements. The XPS results revealed a higher surface Br/Pb atomic ratio for HUM1-PNCs compared to HIM2-PNCs, indicating enhanced surface passivation by Br^- anions (Figure 2c and Figure S9). We attribute this to the different synthesis mechanisms. In conventional HI synthesis, where the halides are supplied via PbX_2 precursors, achieving a halide-rich environment is stoichiometrically constrained. In contrast, the S_N2-based HU synthesis decouples the halide source from the metal precursors (i.e., Cs and Pb), facilitating the generation of abundant OAM–Br species [6]. Consequently, this excess OAM–Br promotes effective in situ Br^- passivation, occupying surface sites vacated by oleate ligands consumed as nucleophiles in the S_N2 reaction.

To rationalize the surface stabilization of HU-PNCs by Br^- passivation, we performed density functional theory (DFT)

16163028, 2026, 75, Downloaded from https://advanced.onlinelibrary.wiley.com/doi/10.1002/adfm.77751 by Hanyang University Library, Wiley Online Library on [08/11/2026]. See the Terms and Conditions (https://onlinelibrary.wiley.com/terms-and-conditions) on Wiley Online Library for rules of use; OA articles are governed by the applicable Creative Commons License

calculations, focusing on the surface passivation and deprotonation behavior of OAM in the presence of Br^- and oleate, respectively. The calculated E_b revealed that the surface model containing cationic OAM and Br^- exhibits a stronger interaction with the $CsPbBr_3$ (100) surface than the model containing OAM and oleate, suggesting that Br^- provides more robust surface binding than oleate (Figure 2d, Figures S10 and S11). Accordingly, Br^- is thermodynamically favored to remain bound on the PNCs during HU synthesis, resulting in dominant Br^- passivation. To further clarify the influence of oleate and Br^- on the interactions of OAM, we investigated the deprotonation tendency of OAM in the presence of oleate and Br^-, respectively. In the oleate system, the deprotonation of OAM was thermodynamically more favorable than that of the Br^- system (Figure S12). This implies that oleate more readily induces the deprotonation of OAM, leading to its conversion into OLA. This difference reflects the intrinsically weak basicity of Br^- compared to oleate. Consistent behavior was also observed on the surface. On the $CsPbBr_3$ surface, oleate was associated with a more favorable deprotonation tendency of OAM than Br^-, whereas Br^- showed a significantly weaker driving force for proton transfer, thereby stabilizing OAM in its cationic form (Figure 2e and Figure S13). As a result, the Br^- passivation effectively stabilized OAM at the surface, suppressing the formation of surface defects in HU-PNCs. Consistent with the theoretical findings, the PL decay lifetime of HUM1-PNCs was longer than that of HIM2-PNCs in the solution-phase time-resolved PL (TR-PL) measurements (Figure S14 and Table S2). This confirms that the robust Br^--driven defect passivation suppresses non-radiative recombination in HU-PNCs [19].

As confirmed in Figure 2 and Note S1, HU-PNCs possess a lower surface ligand density than HI-PNCs, primarily due to the absence of oleate ligands. Nevertheless, HU-PNCs retain colloidal dispersibility in non-polar solvents, stabilized predominantly by cationic OAM organic ligands [6]. To elucidate the effect of solvent interactions on organic ligand density, we employed various solvents of the same volume, including MeOAc, chlorobenzene (CB), and toluene, as anti-solvents during purification process, selected for their different dielectric constants (ε) of 6.68, 5.62, and 2.38, respectively [20]. While HI-PNCs were precipitated by MeOAc under centrifugation (i.e., HIM1-PNCs), they showed only partial precipitation in CB and negligible precipitation in toluene (Figure 3a). The lower the solvent ε, the stronger the van der Waals interactions between the surface ligands and the solvent, thereby preventing the precipitation of HI-PNCs during centrifugation [21, 22]. In contrast, owing to their low organic ligand density, HU-PNCs were precipitated via centrifugation not only using MeOAc (i.e., HUM1-PNCs) but also using less polar solvents such as CB and toluene (denoted as HUC- and HUT-PNCs, respectively) (Figure 3a). These results demonstrate that HU-PNCs can be effectively purified without the use of polar anti-solvent (i.e., MeOAc).

We investigated the optical properties of HUC- and HUT-PNCs and found that they displayed optical features nearly identical to HUM1-PNCs in their UV–Vis absorption and PL spectra (Figure S15). Furthermore, spin-coated thin films of HUC- and HUT-PNCs exhibited RMS roughness values of 6.221 and 6.758 nm, respectively, comparable to the value obtained for HUM1-PNCs (Figure 3b). TGA analysis revealed that HUC- and HUT-PNCs exhibited weight losses of 13.2% and 13.3%, respectively, at 430C, which are consistent with the 12.0% loss of HUM1-PNCs (Figure 3c) [18]. The ^{1}H-NMR spectra confirmed that resonances associated with unreacted precursors were absent in HUC- and HUT-PNCs, identical to the observations for HUM1-PNCs (Figure S16). The FT-IR and ^{13}C-NMR spectra of HUC- and HUT-PNCs also exhibited no signals for carboxylate groups, consistent with the observations for HUM1-PNCs (Figures S17 and S18). Therefore, these results demonstrate that despite employing low-polarity solvents (i.e., CB and toluene) instead of high-polarity MeOAc, efficient removal of long-chain residuals was achieved while simultaneously preserving the intrinsic surface ligand composition and high-quality thin film morphology. Furthermore, the HU-PNC colloidal dispersions retained their initial optical density in the UV–Vis absorption spectra after 4 days of storage, demonstrating a colloidal stability comparable to that of the HIM2-PNC solutions (Figure S19).

Consistent with the observations for HUM1-PNCs shown in Figure 1d, HUC- and HUT-PNCs exhibited higher PLQY values than those of HIM2-PNCs, despite the absence of oleate ligands (Figure S15). To elucidate the origin of this enhanced optical property, we also conducted XPS measurements on HUC- and HUT-PNCs. HUC- and HUT-PNCs showed Br/Pb atomic ratios comparable to those of HUM1-PNCs, which are higher than the ratios of HIM2-PNCs shown in Figure 2c (Figure 3d and Figure S20). These results indicate that the HU-PNC surfaces are stabilized via more robust Br^- passivation compared to those of HI-PNCs. This enhanced passivation leads to the suppression of surface defect formation, consistent with the longer PL decay lifetimes of HU-PNCs observed in solution-phase TR-PL measurements (Figure S21 and Table S3) [19]. Consequently, despite their low ligand density, HU-PNCs exhibited enhanced photophysical properties compared to HI-PNCs, attributed to the robust Br^--driven surface stabilization achieved without the use of polar anti-solvents.

We conducted a detailed characterization of PNC thin films exhibiting high quality and uniform morphology suitable for application as photoactive layers. For this characterization, we selected HUT-PNCs, which exhibited superior optical properties among the purified HU-PNCs, as a representative sample alongside HIM2-PNCs. The HUT-PNC thin films with robust Br^--stabilized surfaces exhibited a PLQY of 65.8%, which is significantly higher than the 40.7% observed for HIM2-PNC thin films (Figure 4a). Furthermore, the HUT-PNC thin films showed a narrower FWHM of 19 nm compared to 21 nm observed for the HIM2-PNC thin films. This improvement is attributed to reduced energetic disorder arising from improved crystal size uniformity, although Br^--mediated passivation, which suppresses sub-bandgap trap states, may also contribute [6, 23]. This is further confirmed by a lower Urbach energy (E_U) of 29.7 meV for HUT-PNC thin films, extracted from the Urbach tail of the absorption spectra, compared to the 37.3 meV obtained for HIM2-PNC thin films (Figure 4b) [23–25].

We also conducted photon energy-dependent TR-PL measurements to investigate their PL decay dynamics [26]. When measured at the photon energy corresponding to PL emission maximum, the HUT-PNC thin films showed a longer PL decay lifetime of 14.72 ns, compared to 7.20 ns for the HIM2-PNC films (Figure 4c). Although both HIM2- and HUT-PNC thin films

16163028, 2026, 75, Downloaded from https://advanced.onlinelibrary.wiley.com/doi/10.1002/adfm.77751 by Hanyang University Library, Wiley Online Library on [08/11/2026]. See the Terms and Conditions (https://onlinelibrary.wiley.com/terms-and-conditions) on Wiley Online Library for rules of use; OA articles are governed by the applicable Creative Commons License

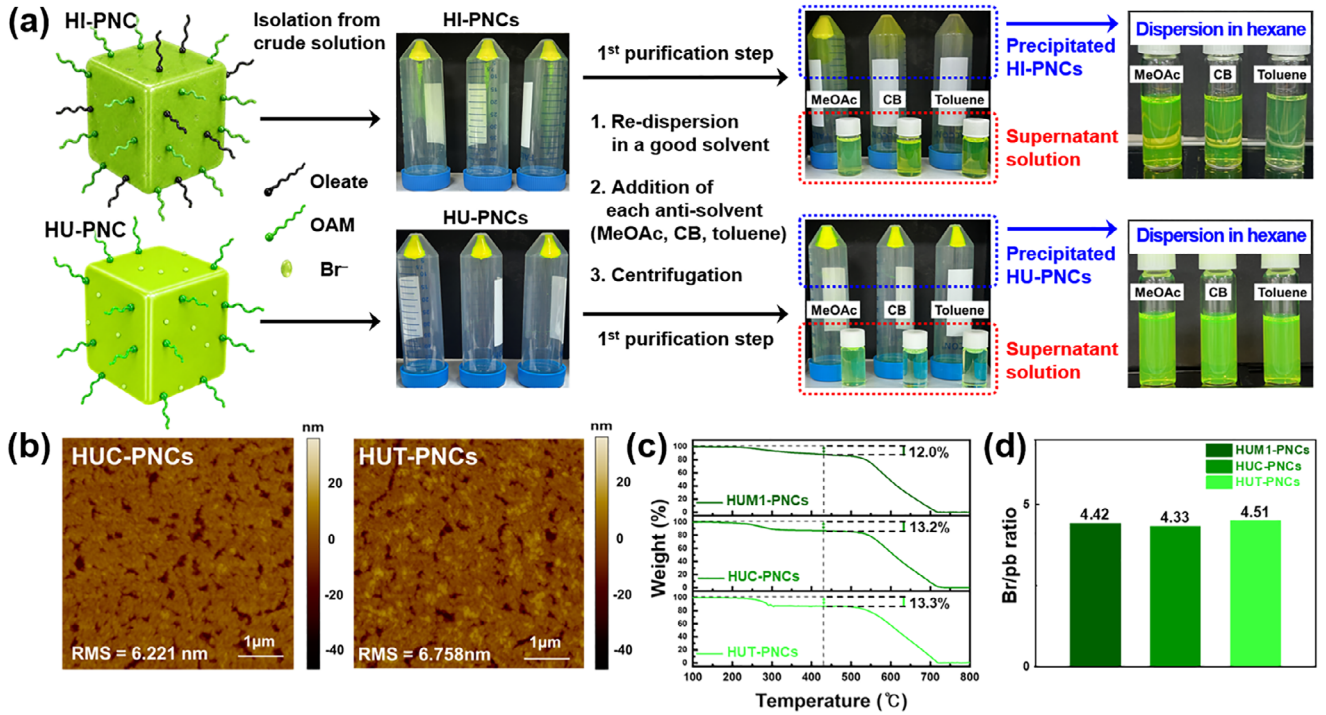

FIGURE 3 | (a) Purification procedures for HI- and HU-PNCs using MeOAc, CB, and toluene. As-synthesized HI- and HU-PNCs were isolated from the crude solutions via centrifugation, purified with each anti-solvent, and finally dispersed in a good solvent. (b) AFM images of spin-cast thin films composed of HUC- and HUT-PNCs, respectively. (c) TGA plots and (d) surface Br/Pb elemental ratios of HUM1-, HUC-, and HUT-PNCs. The data for HUM1-PNCs are identical to those shown in Figure 2a,c. The Br/Pb elemental ratios in (d) were obtained from XPS measurements.

exhibited slower PL decay at lower photon energies (Table S4), the energy dependence of the PL decay lifetime in the HUT-PNC thin films was smaller than that of HIM2-PNC thin films (Figure S22) [26]. These results also confirm that the HUT-PNC thin films exhibit reduced energy disorder compared to HIM2-PNC thin films, attributed to their improved crystal size uniformity and suppressed surface defects [26].

To investigate the crystal orientation and packing structure, we conducted grazing-incidence wide-angle X-ray Scattering (GIWAXS) measurements on HIM2- and HUT-PNC thin films. For the HIM2-PNC thin films, the (100) and (200) diffraction signals of cubic-phase $CsPbBr_3$ ($q_z = 1.1$ and 2.15 $Å^{-1}$, respectively) appeared as isotropic Debye–Scherrer rings, indicating a random crystallite orientation (Figure 4d). In contrast, these signals were concentrated along the out-of-plane direction in the HUT-PNC thin films, indicating a strong preferential orientation. This suggests that the superior crystal siz e uniformity of HUT-PNCs facilitates their self-assembly into orientationally ordered array [27–29]. To investigate the charge transport and trap density (n_t) of PNC thin films, we performed space-charge-limited current (SCLC) measurements on devices incorporating HIM2- and HUT-PNC thin films (see details in Methods). The devices based on HUT-PNCs exhibited a trap-filled limit voltage (V_{TFL}, 0.37 V) and a n_t (1.27×10^{17} cm^{-3}), significantly lower than the values obtained for HIM2-PNC devices (0.47 V and 1.61×10^{17} cm^{-3}, respectively) (Figure 4e). Furthermore, the HUT-PNC devices exhibited an improved charge carrier mobility of 2.59×10^{-6} cm^2 V^{-1} s^{-1}, compared to 7.62×10^{-7} cm^2 V^{-1} s^{-1} observed for the HIM2-PNC devices. These results demonstrate that HUT-PNC thin films exhibit improved inter-PNC electronic coupling compared to HIM2-PNC thin films, attributed to their reduced organic ligand density and enhanced orientational ordering.

We evaluated the device performance by employing these HUT- and HIM2-PNC thin films, passivated with long-chain organic ligands, directly as emissive layers in LED devices, without any ligand exchange process. The LEDs were fabricated with the architecture schematically illustrated in Figure 5a (The detailed fabrication procedures are described in the **Methods**). The corresponding energy-level diagram of the electrodes, charge injection layers, and PNC emissive layers is depicted in Figure S23. The HUT-PNC LEDs exhibit higher current densities compared to the HIM2-PNC devices across the entire applied voltage range, attributed to enhanced charge injection and more efficient charge transport (Figure 5b). These improvements also resulted in a reduced turn-on voltage (V_{on}); the HUT-PNC LEDs exhibited a V_{on} of 2.7 V (defined at 0.1 cd m^{-2}), lower than the 3.0 V observed for the HIM2-PNC devices (Table 1). Moreover, efficient charge injection and transport promote effective radiative recombination, resulting in enhanced luminance and external quantum efficiency (EQE). Specifically, the HUT-PNC LED devices achieved a maximum luminance of 314 cd m^{-2} and a maximum EQE of 11.4%, significantly improving the HIM2-PNC LED, which exhibited values of only 59 cd m^{-2} and 2.7%, respectively (Figure 5c,d, and Table 1). This represents a more than five-fold increase in luminance and a four-fold enhancement in EQE, underscoring the highest performance reported to date among LEDs based on directly integrated PNCs without post-synthetic surface engineering (e.g., ligand exchange, additives) (Table S5). While this performance does not yet surpass that of state-of-the-art devices, it demonstrates the distinctive surface

16163028, 2026, 75, Downloaded from https://advanced.onlinelibrary.wiley.com/doi/10.1002/adfm.77751 by Hanyang University Library, Wiley Online Library on [08/11/2026]. See the Terms and Conditions (https://onlinelibrary.wiley.com/terms-and-conditions) on Wiley Online Library for rules of use; OA articles are governed by the applicable Creative Commons License

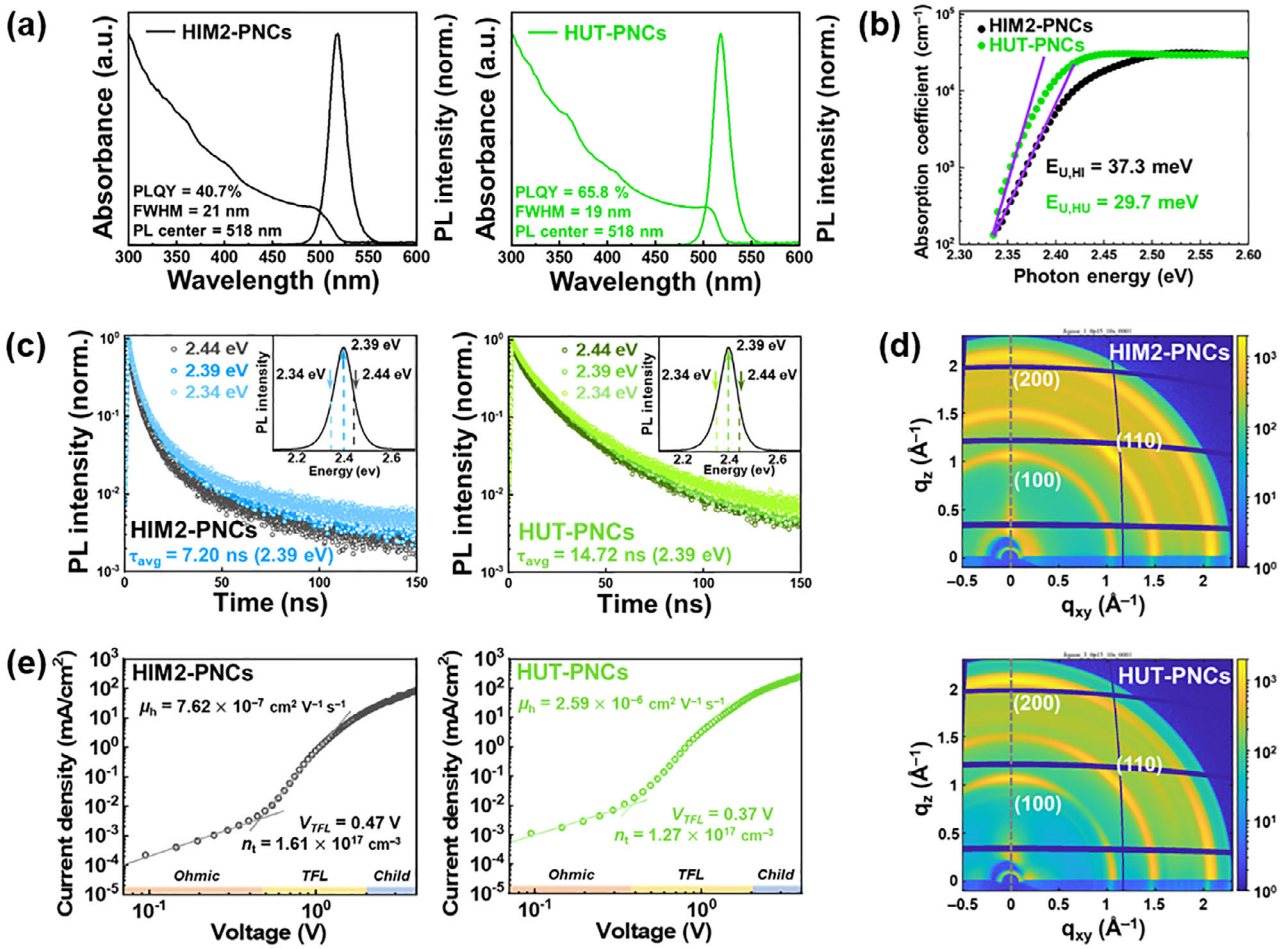

FIGURE 4 | (a) UV–Vis absorption and PL spectra, and (b) Urbach energies of HIM2- and HUT-PNC thin films. (c) TR-PL plots and fitted decay curves for HIM2- and HUT-PNC thin films, excited at 400 nm and measured at various emission energies including PL peak center. (d) GIWAXS patterns of HIM2- and HUT-PNC thin films. (e) SCLC plots of hole-only devices composed of HIM2- and HUT-PNC thin films, respectively.

chemistry of HU-PNCs, differing them from conventional HI-PNCs; specifically, their low ligand density and Br^--rich surface passivation allow for direct incorporation into LED devices without the need for ligand exchange process. Additionally, the statistical distribution of EQE values, collected from each 15 device for both the HIM2- and HUT-PNCs demonstrates the high device performance reproducibility of the HUT-PNC LEDs (Figure S24). To further evaluate device durability, operational lifetime measurements were conducted under a constant initial luminance of ~50 cd m^{-2}. The HUT-PNC LEDs exhibited a T_{50} approximately 2.3 times longer than that of HIM2-PNC LEDs (Figure S25). This prolonged lifetime indicates that the robust Br^--mediated surface passivation effectively suppresses trap density, thereby enhancing the operational stability of the devices.

We also evaluated the spectral characteristics of the devices. The electroluminescence (EL) spectra demonstrate that the HUT-PNC LEDs exhibit a narrower FWHM of 17 nm compared to 21 nm observed for the HIM2-PNC LEDs (Figure 5e and Table 1). This narrow FWHM indicates a high color purity of HUT-PNC LEDs, which is evidenced by the CIE coordinates in Figure 5f. The excellent EL spectral characteristics of the HUT-PNC LEDs are mainly attributed to the highly monodisperse HU-PNCs synthesized via S_N2-based heat-up synthesis [6]. Furthermore, the effective surface passivation mediated by Br^- suppresses the trap density and may reduce sub-bandgap trap states, thereby minimizing inhomogeneous broadening and contributing to the narrower FWHM. The HU-PNC LEDs benefit from synergistic combination of defect-minimized, uniform PNCs and a reduced organic ligand density. This effectively minimizes insulating barriers at the interfaces between neighboring PNCs, thereby facilitating enhanced charge injection as illustrated in Figure 5g. Consequently, these synergistic effects between their surface chemistry and morphological uniformity enable high color purity and device operation in the absence of post-synthetic ligand exchange process, in contrast to conventional PNC-based LEDs that rely on the additional process (Figure S26). These results highlight the potential of HU-PNCs, with their distinctive surface chemistry, as a platform material.

3 | Conclusions

We demonstrated that a surface chemistry with a low ligand density and robust halide passivation enables colloidal PNCs to operate in optoelectronic devices without complex ligand exchange processes. The HU-PNCs, synthesized via the S_N2-based

16163028, 2026, 75, Downloaded from https://advanced.onlinelibrary.wiley.com/doi/10.1002/adfm.77751 by Hanyang University Library, Wiley Online Library on [08/11/2026]. See the Terms and Conditions (https://onlinelibrary.wiley.com/terms-and-conditions) on Wiley Online Library for rules of use; OA articles are governed by the applicable Creative Commons License

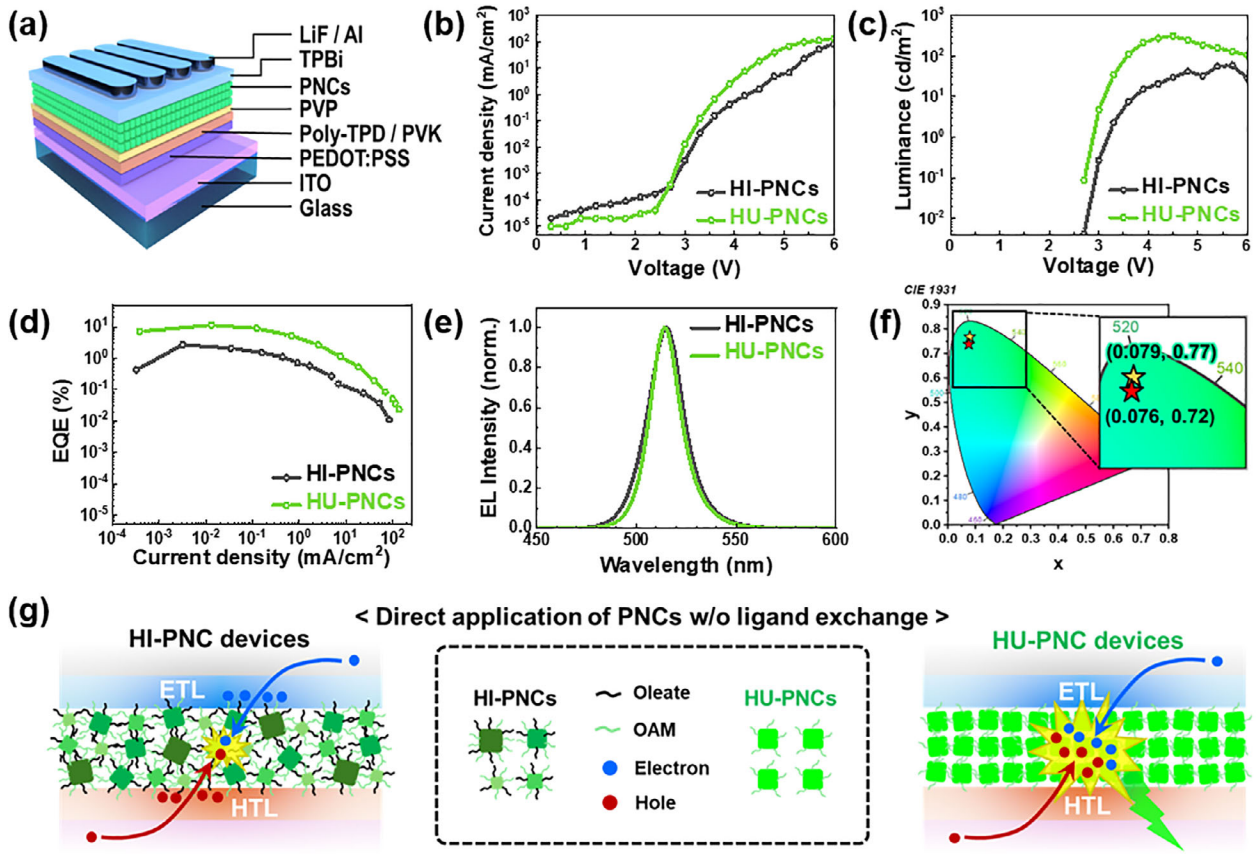

FIGURE 5 | (a) Schematic illustration depicting device structure of HI- and HU-PNC LEDs. (**b**) *J–V*, (**c**) *L–V*, and (**d**) EQE–*J* curves of HI- and HU-PNC LEDs. (**e**) Normalized EL spectra and (**f**) CIE chromaticity diagram of HI- and HU-PNC LEDs (red and yellow stars, respectively). (**g**) Schematic illustration showing charge carrier injection behaviors in HI- and HU-PNC LEDs.

heat-up method, exhibited a low ligand density arising from the absence of oleate ligands, being stabilized instead by robust Br^- passivation. Our findings reveal that the OAM/Br^- ligand system on the $CsPbBr_3$ (100) facet exhibits a stronger binding than the conventional OAM/oleate system, resulting in the suppression of surface defect formation in HU-PNCs compared to HI-PNCs. This led to enhanced PLQY and a narrower emission bandwidth. The HU-PNC thin films exhibited superior charge carrier mobility and suppressed energetic disorder compared to HI-PNC thin films, attributed to their low ligand density and enhanced crystal size uniformity. Owing to their low ligand density and Br^--rich surface chemistry, HU-PNCs can be directly incorporated into LED devices without complex ligand exchange processes, achieving an EQE_{max} of 11.4% and high color purity. With their unique surface chemistry, which is fundamentally different from that of conventional HI-PNCs, HU-PNCs emerge as a highly versatile platform material for a wide range of device applications, particularly enabling direct device integration.

4 | Methods

4.1 | Materials

Cesium carbonate (Cs_2CO_3, 99.99%), oleic acid (OA, technical grade 90%), toluene (99.8%, anhydrous), 1-octadecene (ODE, technical grade 90%), lead (II) bromide ($PbBr_2$, 99.999%), and lead (II) acetate trihydrate ($Pb(OAc)_2{\cdot}3H_2O$, 99.995%) were purchased from Alfa Aesar. Chlorobenzene (99.9%) was purchased from Samchun Chemicals. Methyl acetate (MeOAc, 99.9%, Extra Pure) was purchased from DaeJung Chemicals & Metals. Lead (II) oxide (PbO, ≥99.9%), oleylamine (OLA, technical grade 70%), 1-octylbromide (Br-8, 99%), dimethyl sulfoxide-d_6 (DMSO-d_6, 99.9 atom% D), chloroform-*d* (99.8 atom% D, contains 0.03 volume% TMS), poly(9-vinylcarbazole) (PVK, M_w = 1100 kDa), and polyvinylpyrrolidone (PVP, M_w = 40 kDa) were purchased from Sigma Aldrich. Indium tin oxide-based transparent electrode (ITO, ≈4.5 Ω sq^{-1}) was purchased from AMG. An aqueous solution of poly(3,4-ethylenedioxythiophene) polystyrene sulfonate (PEDOT: PSS) (Clevios AI 4083) was purchased from Heraeus. Poly(N,N'-bis-4-butylphenyl-N,N'-bisphenyl)benzidine (poly-TPD, M_w = 40 kDa) was purchased from Ossila. Molybdenum trioxide (MoO_3, 99.9995%) was purchased from Alfa Aesar. 2,2′,2″-(1,3,5-benzinetriyl)tris(1-phenyl-1-H-benzimidazole) (TPBi; 99.9%) was purchased from OSM. LiF (99.9%), Al (99.9%) and Ag (99.99%) were purchased from iTASCO.

4.2 | S_N2-Based Heat-Up Synthesis of $CsPbBr_3$ PNCs

The S_N2-based heat-up synthesis is based on the synthesis method proposed by Kim et al. [6]. First, Cs(oleate) stock solution

16163028, 2026, 75, Downloaded from https://advanced.onlinelibrary.wiley.com/doi/10.1002/adfm.77751 by Hanyang University Library, Wiley Online Library on [08/11/2026]. See the Terms and Conditions (https://onlinelibrary.wiley.com/terms-and-conditions) on Wiley Online Library for rules of use; OA articles are governed by the applicable Creative Commons License

TABLE 1 | Summarized device performances of champion devices composed of HI- and HU-PNCs.

Sample configuration	L_{max} (cd m^{-2}) @ bias	EQE_{max} (%) @ bias	Turn-on Voltage (V) @ 0.1 cd m^{-2}	Wavelength (nm)	FWHM (nm)
HI-PNCs	59@5.7	2.7@3.0	3.0	515	21
HU-PNCs	314@4.5	11.4@3.0	2.7	514	17

was prepared by dissolving 3.258 g (10 mmol) of Cs_2CO_3 in 28.41 mL of OA at 120°C under vacuum. $Pb(oleate)_2$ stock solution was prepared by dissolving 2.232 g (10 mmol) of PbO in 10 mL of OA at 120°C under vacuum. These stock solutions were purged with an inert Ar gas and then cooled to room temperature for storage and usage. To synthesize the $CsPbBr_3$ PNCs, 17.3 mL of Br-8, 10 mL of OLA, 0.6 mL of OA, 0.28 mL of Cs(oleate) stock solution (containing 0.2 mmol of Cs(oleate)), and 1.8 mL of $Pb(oleate)_2$ stock solution (containing 1.8 mmol of $Pb(oleate)_2$) were homogeneously blended in a single reactor. The precursor solutions were rapidly heated up to 120°C and maintained for 5 min, followed by cooling to room temperature. After adding some toluene to prevent the freezing of the crude solutions, the as-synthesized HU-$CsPbBr_3$-PNCs were collected from the diluted crude solutions using ultra-speed centrifugation (over 10,000 rpm). The collected HU-$CsPbBr_3$-PNCs were dispersed in 5 mL of toluene (hexane can be mixed for smooth dispersion) before one of the desired purification processes mentioned below. The $Pb(oleate)_2$ stock solution solidifies readily at room temperature and is challenging to handle. If the use of the $Pb(oleate)_2$ stock solution is not preferred, the $Pb(oleate)_2$ solution can instead be formed by adding the same molar quantity of PbO or $Pb(OAc)_2$ and OA to the reactor, identical to the original molar amount of the $Pb(oleate)_2$ stock solution added. Following this, the S_N2-based heat-up synthesis can be performed by adding Cs(oleate), OA, OLA, and Br-8 at room temperature.

4.3 | Hot-Injection Synthesis of $CsPbBr_3$ PNCs

The HI-$CsPbBr_3$-PNCs were synthesized following the methods previously reported by Swarnkar et al. [16]. Briefly, Cs(oleate) stock solution for the hot-injection synthesis was first prepared by dissolving 0.4078 g of Cs_2CO_3 in 20 mL of ODE and 1.25 mL of OA at 120°C under vacuum and then purging with an inert Ar gas at 90°C before usage. For synthesis, 0.4 g of $PbBr_2$, 25 mL of ODE, 2.5 mL of OA, and 2.5 mL of OLA were input in a flask and dissolved at 120°C under vacuum. After being purged with an inert Ar gas and heated up to 180°C, 2 mL of Cs(oleate) stock solution was injected into the $PbBr_2$-dissolved solution, followed by rapid cooling to room temperature with an ice bath. After adding some toluene to prevent the freezing of the crude solutions, the as-synthesized HI-$CsPbBr_3$-PNCs were collected from the diluted crude solutions using ultra-speed centrifugation (over 10,000 rpm). The collected HI-$CsPbBr_3$-PNCs were dispersed in 5 mL of toluene (hexane can be mixed for smooth dispersion) before one of the desired purification processes mentioned below.

4.4 | Conventional Purification Method Using MeOAc

The use of MeOAc solvent for PNC purification was first proposed by Swarnkar et al. [16]. For the purification using MeOAc, the collected HI- and HU-PNC solutions dispersed in 5 mL of toluene were first mixed with 5 mL of MeOAc and then centrifuged at 8,000 rpm. The precipitated HI- and HU-PNCs were re-dispersed in 5 mL of toluene (i.e., HIM1- and HUM1-PNCs, respectively). The HIM1- and HUM1-PNC solutions were mixed with 5 mL of MeOAc a second time and then centrifuged at 8,000 rpm. The precipitated HI- and HU-PNCs were re-dispersed in 3 mL of toluene (i.e., HIM2- and HUM2-PNCs, respectively). Hexane can be mixed for smooth dispersion. Undesirably aggregated PNCs can be removed by centrifugation at 5,000 rpm.

4.5 | Purification Using Non-Polar Solvents

For the purification of HU-PNCs using non-polar solvents, the collected HU-PNC solutions dispersed in 5 mL of toluene were mixed with 5 mL of non-polar solvents (e.g., CB and toluene, respectively) and subsequently centrifuged at 8000 rpm. The precipitated HU-PNCs were re-dispersed in 3 mL of toluene (i.e., HUC- and HUT-PNCs, respectively). Hexane can be mixed for smooth dispersion. Unwantedly aggregated PNCs can be removed by centrifugation at 5000 rpm.

4.6 | LED Device Fabrication

The LED device architecture was composed of indium tin oxide (ITO)/PEDOT:PSS/PVK + poly-TPD/PVP/PNCs/TPBi/LiF/Al. For the application of LED devices, the ITO substrate was washed with DI water, acetone, and isopropyl alcohol for 10 min each with ultrasonication. After drying, the ITO substrates were treated with O_2 plasma for 30 min. The aqueous PEDOT:PSS solution was spin-coated on ITO at 4,500 rpm for 40 s and annealed at 145°C on the hotplate for 10 min. The mixture solution of PVK and poly-TPD was prepared by dissolving them in CB at a concentration of 6 mg/mL with a 1:1 weight ratio. The mixture solution was spin-coated onto the PEDOT:PSS layer at 4000 rpm for 40 s and subsequently annealed at 140°C for 10 min in the N_2-filled glove box. Following this, a PVP solution dissolved in isopropyl alcohol (0.3 mg/mL) was spin-coated at 3000 rpm for 30 s and annealed at 130°C for 10 min. To fabricate the HI- and HU-PNC LEDs, HIM2- and HUT-PNCs were used as the emissive layers, respectively. HI- and HU-PNC solutions (7 and 20 mg/mL in octane, respectively) were spin-coated at 2000 rpm for 20 s,

16163028, 2026, 75, Downloaded from https://advanced.onlinelibrary.wiley.com/doi/10.1002/adfm.77751 by Hanyang University Library, Wiley Online Library on [08/11/2026]. See the Terms and Conditions (https://onlinelibrary.wiley.com/terms-and-conditions) on Wiley Online Library for rules of use; OA articles are governed by the applicable Creative Commons License

without any additional post-synthetic ligand exchange processes. TPBi (40 nm), LiF (1 nm), and Al (100 nm) were sequentially deposited at ≈10^{-6} Torr by the thermal evaporator.

4.7 | Characterizations

UV–Vis absorption spectroscopy was carried out using a V-770 UV–Vis spectrophotometer (Jasco). Steady-state PL spectra were measured using a Spectrophotometer FS5 (Edinburgh), and PL features (i.e., FWHM and PLQY) were obtained using Fluoracle software (Edinburgh). The samples were excited using a 400 nm wavelength, and PLQY was measured using an integrating sphere. The TR-PL measurements were performed on the DeltaPro fluorescence lifetime system (Horiba FluoroMax Plus), where a laser with an excitation wavelength of 370 nm was used. Atomic force microscopy (AFM) images were measured using a Park System NX10 microscope with non-contact mode. Optical microscopy images were obtained using an Olympus BX53M upright microscope. HR-TEM images were obtained using a JEM 2100F transmission electron microscope (JEOL). TGA measurements were carried out on a Q50 TA instrument in a N_2 atmosphere with a heating speed of 5 °C/min. ^{1}H- and ^{13}C-NMR spectroscopy were performed using a 400 MHz Fourier transform nuclear magnetic resonance (FT-NMR) spectrometer. All ^{1}H- and ^{13}C-NMR samples were prepared by dissolving vacuum-dried PNCs in DMSO-d_6 at a concentration of 75 mg/mL. The ^{1}H-NMR spectra were collected with 16 scans and referenced to tetramethylsilane (0 ppm). The ^{13}C-NMR spectra were acquired with 500 scans. X-ray photoelectron spectroscopy (XPS) was performed using a UVP, Inc. NEXSA G2 analyzer, and elemental compositions were calculated from XPS spectra using a UVP, Inc. Advantage data system. Fourier-transform infrared (FT-IR) spectra were recorded using a Thermo Fisher Scientific Nicolet iS20 FT-IR spectrometer. Grazing-incidence wide-angle X-ray scattering (GIWAXS) measurements were performed at the 3C beamline of the Pohang Accelerator Laboratory (PAL) in Republic of Korea. For the evaluation of LED device performances, current density–voltage–luminance (*J–V–L*) characteristics were measured using a Konica Minolta spectroradiometer (CS-2000) with a Keithley 2450 source meter. All LED measurements were performed in an N_2-filled glovebox without encapsulation.

4.8 | SCLC Measurement

SCLC curves were measured under dark conditions. The hole mobility was calculated from the Mott-Gurney formula in the Child region of SCLC curves as follows [30]:

$$J = \frac{9\mu\varepsilon_0\varepsilon_r V^2}{8d^3}$$

where J is the current density, μ is the charge carrier mobility, ε_0 is the absolute permittivity, ε_r is the dielectric constant of cubic α-phase $CsPbBr_3$ ($\varepsilon_r = 7.3\varepsilon_0$), V is the applied voltage and d is the film thickness of the $CsPbBr_3$ PNC layer [31]. The trap density of hole was calculated from the equation using trap-filled limited voltage (V_{TFL}) as follows [32]:

$$V_{TFL} = \frac{qn_t d^2}{2\varepsilon_0\varepsilon_r}$$

where q is the elementary charge, n_t is the trap density, and d is the film thickness of the $CsPbBr_3$ PNC layer. The hole-only devices for SCLC measurements were constructed by ITO/PEDOT:PSS/poly-TPD + PVK/PNCs/MoO_x/Ag.

4.9 | DFT Calculations

The DFT calculations were performed to investigate the characteristics of OAM^+–$oleate^-$ and OAM^+–Br^- in PNCs. All calculations were carried out with the DMol^3 program [33, 34]. The generalized gradient approximation with the Perdew-Burke-Ernzerhof functional was employed for the exchange-correlation energy [35]. Spin-polarized calculations were employed and Tkatchenko-Scheffler method [36] was used for dispersion corrections. All electron core treatment and a double numerical plus polarization basis set (version 4.4) were used for the core electrons and atomic basis set, respectively. The geometry optimizations were performed with convergence criteria of 2.0×10^{-5} Ha for energy, 0.004 Ha/Å for force, 0.005 Å for atomic displacement, and 1.0×10^{-5} Ha for self-consistent field. The orbital cut-off was defined as 5.1 and 3.7 Å for periodic systems and molecular systems, respectively. The (100) surface of $CsPbBr_3$ perovskite was considered for our DFT calculations. Moreover, CsBr–termination was considered to investigate the binding characteristics of OAM^+–$oleate^-$ and OAM^+–Br^-. The surface model systems were optimized using gamma k-point with a Monkhorst–Pack grid [37]. Furthermore, the unit cell of $CsPbBr_3$ was optimized with $8 \times 8 \times 8$ k-points.

The binding energies (E_b) were calculated by using the following equation:

$$E_b = E_{total} - (E_{surface} + E_{molecule})$$

where E_{total}, $E_{surface}$, and $E_{molecule}$ are the energy of the total system, the energy of the (100) surface of $CsPbBr_3$ with CsBr vacancy, and the energy of ligand molecule, respectively.

The formation energy of deprotonation reaction was calculated by using the following equation:

$$\text{Formation energy} = E_{product} - E_{reactant}$$

where $E_{product}$ and $E_{reactant}$ are the energy of product system and the energy of reactant system, respectively.

Author Contributions

Donghun Lee: investigation, formal analysis. **Dong Gyu Lee**: formal analysis, visualization, writing – original draft, software. **Huieun Kim**: investigation, visualization, formal analysis. **Wondo Choi**: investigation, formal analysis. **Gyeong Eun Seok**: investigation, writing – original draft, validation, visualization, methodology, formal analysis, data curation. **Jigeon Kim**: conceptualization, investigation, methodology, validation, visualization, data curation, writing – original draft, writing – review and editing, formal analysis. **Wooyeon Kim**: investigation, formal analysis. **Yubin Lee**: conceptualization, investigation, writing – original draft, methodology, validation, visualization, data curation, formal analysis. **Younghoon Kim**: supervision, conceptualization, investigation, funding

16163028, 2026, 75, Downloaded from https://advanced.onlinelibrary.wiley.com/doi/10.1002/adfm.77751 by Hanyang University Library, Wiley Online Library on [08/11/2026]. See the Terms and Conditions (https://onlinelibrary.wiley.com/terms-and-conditions) on Wiley Online Library for rules of use; OA articles are governed by the applicable Creative Commons License

acquisition, writing – original draft, writing – review and editing, visualization, methodology, validation, formal analysis, project administration. **Min Jae Ko**: investigation, formal analysis. **Seongwon Lee**: visualization, formal analysis, software. **Tae Kyung Lee**: writing – original draft, writing – review and editing, software, formal analysis, investigation, visualization, methodology. **Jinhan Cho**: investigation, formal analysis. **Woo Hyeon Jeong**: investigation, formal analysis. **Won Bin Im**: investigation, formal analysis. **Bo Ram Lee**: supervision, conceptualization, investigation, writing – original draft, funding acquisition, methodology, validation, visualization, writing – review and editing, formal analysis, project administration. **Sung Woo Jang**: investigation, formal analysis.

Acknowledgements

This was supported by the National Research Foundation of Korea (NRF) funded by Ministry of Science and ICT (RS-2026-25538589). This work was supported by the Technology Innovation Program Development Program funded by the Ministry of Trade, Industry & Energy (MOTIE) (RS-2023-00265858). This work was also supported by the Korea Basic Science Institute (National Research Facilities and Equipment Center) grant funded by the Ministry of Science and ICT (RS-2024-00403217). This work was supported by National Research Foundation of Korea (NRF) grants funded by the Korea government (MSIT) (RS-2025-00523067).

Conflicts of Interest

The authors declare no conflicts of interest.

Data Availability Statement

The data that support the findings of this study are available from the corresponding author upon reasonable request.

References

1. Y. Shirasaki, G. J. Supran, M. G. Bawendi, and V. Bulović, "Emergence of Colloidal Quantum-Dot Light-Emitting Technologies," *Nature Photonics* 7 (2013): 13–23, https://doi.org/10.1038/nphoton.2012.328.

2. M. A. Boles, D. Ling, T. Hyeon, and D. V. Talapin, "The Surface Science of Nanocrystals," *Nature Materials* 15 (2016): 141–153, https://doi.org/10.1038/nmat4526.

3. L. Hu, Q. Zhao, S. Huang, et al., "Flexible and Efficient Perovskite Quantum Dot Solar Cells via Hybrid Interfacial Architecture," *Nature Communications* 12 (2021): 466, https://doi.org/10.1038/s41467-020-20749-1).

4. M. V. Kovalenko, L. Protesescu, and M. I. Bodnarchuk, "Properties and Potential Optoelectronic Applications of Lead Halide Perovskite Nanocrystals," *Science* 358 (2017): 745–750, https://doi.org/10.1126/science.aam7093.

5. J. Lim, M. T. Hörantner, N. Sakai, et al., "Elucidating the Long-Range Charge Carrier Mobility in Metal Halide Perovskite Thin Films," *Energy & Environmental Science* 12 (2019): 169–176, https://doi.org/10.1039/C8EE03395A).

6. J. Kim, W. Kim, J. I. L. Jang, et al., "SN2-Mediated Decoupled Precursor Provision Enables Large-Scale Production of Monodisperse Lead Halide Perovskite Quantum Dots in a Single Reactor," *Advanced Composites and Hybrid Materials* 8 (2025): 125, https://doi.org/10.1007/s42114-025-01229-w).

7. X. Mei, D. Jia, J. Chen, S. Zheng, and X. Zhang, "Approaching High-Performance Light-Emitting Devices Upon Perovskite Quantum Dots: Advances and Prospects," *Nano Today* 43 (2022): 101449, https://doi.org/10.1016/j.nantod.2022.101449.

8. G. Almeida, L. Goldoni, Q. Akkerman, et al., "Role of Acid–Base Equilibria in the Size, Shape, and Phase Control of Cesium Lead Bromide Nanocrystals," *ACS Nano* 12 (2018): 1704–1711, https://doi.org/10.1021/acsnano.7b08357.

9. Y. Kim and T. Lee, "Engineering Colloidal Perovskite Nanocrystals and Devices for Efficient and Large-Area Light-Emitting Diodes," *Accounts of Materials Research* 4 (2023): 655–667, https://doi.org/10.1021/accountsmr.3c00039.

10. Y.-H. Kim, C. Wolf, Y.-T. Kim, et al., "Highly Efficient Light-Emitting Diodes of Colloidal Metal–Halide Perovskite Nanocrystals Beyond Quantum Size," *ACS Nano* 11 (2017): 6586–6593, https://doi.org/10.1021/acsnano.6b07617.

11. V. K. Ravi, P. K. Santra, N. Joshi, et al., "Origin of the Substitution Mechanism for the Binding of Organic Ligands on the Surface of CsPbBr3 Perovskite Nanocubes," *The Journal of Physical Chemistry Letters* 8 (2017): 4988–4994, https://doi.org/10.1021/acs.jpclett.7b02192.

12. J. Kim, T. Kwon, and Y. Kim, "Surface Manipulation and Engineering Strategies for High-Performance and Multi-Functional Perovskite Colloidal Quantum Dot Solar Cells," *Chemical Engineering Journal* 498 (2024): 155674, https://doi.org/10.1016/j.cej.2024.155674.

13. Y.-K. Wang, F. Yuan, Y. Dong, et al., "All-Inorganic Quantum-Dot LEDs Based on a Phase-Stabilized α-CsPbI 3 Perovskite," *Angewandte Chemie International Edition* 60 (2021): 16164–16170, https://doi.org/10.1002/anie.202104812).

14. J. Shamsi, A. S. Urban, M. Imran, L. Trizio, and L. Manna, "Metal Halide Perovskite Nanocrystals: Synthesis, Post-Synthesis Modifications, and Their Optical Properties," *Chemical Reviews* 119 (2019): 3296–3348, https://doi.org/10.1021/acs.chemrev.8b00644.

15. H. Li, G. Zhao, B. Song, et al., "Evolution of Perovskite Nanocrystals in Hot Injection Process With Various Ligand-rich Systems," *Journal of Sol-Gel Science and Technology* 113 (2025): 11–22, https://doi.org/10.1007/s10971-024-06507-5).

16. A. Swarnkar, A. R. Marshall, E. M. Sanehira, et al., "Quantum Dot–Induced Phase Stabilization of α-CsPbI 3 Perovskite for High-Efficiency Photovoltaics," *Science* 354 (2016): 92–95, https://doi.org/10.1126/science.aag2700.

17. J. Xue, J.-W. Lee, Z. Dai, et al., "Surface Ligand Management for Stable FAPbI3 Perovskite Quantum Dot Solar Cells," *Joule* 2 (2018): 1866–1878, https://doi.org/10.1016/j.joule.2018.07.018.

18. S. Wang, Q. Zhao, A. Hazarika, et al., "Thermal Tolerance of Perovskite Quantum Dots Dependent on A-Site Cation and Surface Ligand," *Nature Communications* 14 (2023): 2216, https://doi.org/10.1038/s41467-023-37943-6.

19. K. H. Lee, S. B. Kim, D. Lee, et al., "Enhanced Visible-Light Photocatalytic CO2 Reduction of Perovskite Nanocrystals via Interfacial Acid Reaction," *Small* (2025): 11806, https://doi.org/10.1002/smll.202511806.

20. W. Chen, L. Hu, Y. Wang, L. Huang, Z. Wang, and X. Tang, "Surface Passivation Strategies for CsPbBr3 Quantum Dots Aiming at Nonradiative Suppression and Enhancement of Electroluminescent Light-Emitting Diodes," *Dalton Transactions* 54 (2025): 2156–2165, https://doi.org/10.1039/D4DT02705A).

21. C. Reichardt and T. Welton, ed., "Empirical Parameters of Solvent Polarity" in *Solvents and Solvent Effects in Organic Chemistry*, (Wiley, 2011): 359–424, https://doi.org/10.1002/9783527632220.

22. A. Cangiano, N. Gallucci, A. Giarra, et al., "Impact of Solvent and Ligand Density on the Self-Assembly and Optical Properties of Metal Nanocrystals," *Nanoscale* 17 (2025): 15829–15840, https://doi.org/10.1039/D5NR01560J).

23. J. De Roo, N. Yazdani, E. Drijvers, et al., "Probing Solvent–Ligand Interactions in Colloidal Nanocrystals by the NMR Line Broadening," *Chemistry of Materials* 30 (2018): 5485–5492, https://doi.org/10.1021/acs.chemmater.8b02523.

24. M. Liu, O. Voznyy, R. Sabatini, et al., "Hybrid Organic–Inorganic Inks Flatten the Energy Landscape in Colloidal Quantum Dot Solids," *Nature Materials* 16 (2017): 258–263, https://doi.org/10.1038/nmat4800.

25. V. Sa-Yakanit and H. R. Glyde, "Urbach Tails and Disorder," *Comments Matter Phys* 13 (1987): 35–48.

16163028, 2026, 75, Downloaded from https://advanced.onlinelibrary.wiley.com/doi/10.1002/adfm.77751 by Hanyang University Library, Wiley Online Library on [08/11/2026]. See the Terms and Conditions (https://onlinelibrary.wiley.com/terms-and-conditions) on Wiley Online Library for rules of use; OA articles are governed by the applicable Creative Commons License

26. S. John, C. Soukoulis, M. H. Cohen, and E. N. Economou, "Theory of Electron Band Tails and the Urbach Optical-Absorption Edge," *Physical Review Letters* 57 (1986): 1777–1780, https://doi.org/10.1103/PhysRevLett.57.1777.

27. A. Swarnkar, R. Chulliyil, V. K. Ravi, M. Irfanullah, A. Chowdhury, and A. Nag, "Colloidal CsPbBr3 Perovskite Nanocrystals: Luminescence Beyond Traditional Quantum Dots," *Angewandte Chemie* 127 (2015): 15644–15648, https://doi.org/10.1002/ange.201508276).

28. C. B. Murray, C. R. Kagan, and M. G. Bawendi, "Synthesis and Characterization of Monodisperse Nanocrystals and Close-Packed Nanocrystal Assemblies," *Annual Review of Materials Research* 30 (2000): 545–610, https://doi.org/10.1146/annurev.matsci.30.1.545.

29. J. A. Vigil, B. M. Wieliczka, B. W. Larson, et al., "Orientational Order in Spin-Cast Lead-Iodide Perovskite Nanocrystal Solids," *Chemistry of Materials* 35 (2023): 9924–9934, https://doi.org/10.1021/acs.chemmater.3c01636.

30. R. Han, Q. Zhao, J. Su, et al., "Role of Methyl Acetate in Highly Reproducible Efficient CsPbI3 Perovskite Quantum Dot Solar Cells," *The Journal of Physical Chemistry C* 125 (2021): 8469–8478, https://doi.org/10.1021/acs.jpcc.0c09057.

31. W. Shcherbakov-Wu, P. C. Sercel, F. Krieg, M. V. Kovalenko, and W. A. Tisdale, "Temperature-Independent Dielectric Constant in CsPbBr3 Nanocrystals Revealed by Linear Absorption Spectroscopy," *The Journal of Physical Chemistry Letters* 12 (2021): 8088–8095, https://doi.org/10.1021/acs.jpclett.1c01822.

32. D. Shi, V. Adinolfi, R. Comin, et al., "Low Trap-State Density and Long Carrier Diffusion in Organolead Trihalide Perovskite Single Crystals," *Science* 347 (2015): 519–522, https://doi.org/10.1126/science.aaa2725.

33. B. Delley, "An All-Electron Numerical Method for Solving the Local Density Functional for Polyatomic Molecules," *The Journal of Chemical Physics* 92 (1990): 508–517, https://doi.org/10.1063/1.458452).

34. B. Delley, "From Molecules to Solids With the DMol3 Approach," *The Journal of Chemical Physics* 113 (2000): 7756–7764, https://doi.org/10.1063/1.1316015).

35. J. P. Perdew, K. Burke, and M. Ernzerhof, "Generalized Gradient Approximation Made Simple," *Physical Review Letters* 77 (1996): 3865–3868, https://doi.org/10.1103/PhysRevLett.77.3865.

36. A. Tkatchenko and M. Scheffler, "Accurate Molecular Van Der Waals Interactions From Ground-State Electron Density and Free-Atom Reference Data," *Physical Review Letters* 102 (2009): 073005, https://doi.org/10.1103/PhysRevLett.102.073005.

37. H. J. Monkhorst and J. D. Pack, "Special Points for Brillouin-Zone Integrations," *Physical Review B* 13 (1976): 5188–5192, https://doi.org/10.1103/PhysRevB.13.5188.

Supporting Information

Additional supporting information can be found online in the Supporting Information section.

Supporting File: adfm77751-sup-0001-SuppMat.docx.

16163028, 2026, 75, Downloaded from https://advanced.onlinelibrary.wiley.com/doi/10.1002/adfm.77751 by Hanyang University Library, Wiley Online Library on [08/11/2026]. See the Terms and Conditions (https://onlinelibrary.wiley.com/terms-and-conditions) on Wiley Online Library for rules of use; OA articles are governed by the applicable Creative Commons License